



Peridynamics Modeling of a Shock Wave Perturbation Decay Experiment in Granular Materials with Intra-granular Fracture

M. Behzadinasab¹ · T. J. Vogler² · A. M. Peterson³ · R. Rahman^{4,5} · J. T. Foster^{1,4}

Received: 29 May 2018 / Accepted: 25 August 2018 / Published online: 30 August 2018
© Society for Experimental Mechanics, Inc 2018

Abstract

The shock wave perturbation decay experiment is a technique in which the evolution of a perturbation in a shock wave front is monitored as it propagates through a material field. This tool has recently been explored to probe the high-rate shear response of granular materials. This dynamic behavior is complicated due to inter- and intra-granular phenomena involved. Mesoscale modeling can give insight into this complexity by explicitly resolving the interactions and deformation of individual grains. The peridynamic theory, which is a nonlocal continuum theory, provides a suitable framework for modeling dynamic problems involving fracture. Prior research has focused mostly on the continuum, bulk response, neglecting any localized material failure, of granular materials. A systematic investigation of the effects of grain fracture and frictional contact forces between grains on the continuum behavior of granular materials is carried out by peridynamic simulations of a shock wave perturbation decay experiment. A sensitivity assessment of dominant factors indicates that grain fracture, a phenomenon ignored in most computational investigations of granular materials, plays a large role in the bulk dynamic response. Our results show that the wave propagates faster with an increase in the toughness of the material and the inter-particle friction. Also, the shock amplitude is shown to decay faster in tougher materials. It is further confirmed that under strong compression self-contact among fractured grain sub-particles cannot be neglected.

Keywords Shock loading · Perturbation decay experiment · Granular materials · Mesoscale modeling · Peridynamics · Fracture · Contact · Friction

Introduction

The shock perturbation decay experiment was proposed by Sakharov et al. [1] as a means to investigate the stability of a shock front and, later, to infer the viscosity of a shocked material. That study and others [2–7] have investigated the dynamic behavior of aluminum, lead, sodium chloride,

water, mercury, and other materials. More recently, researchers in China [8–13] have modified the approach for use with a two-stage gas gun and applied it to aluminum and iron. Vogler [14, 15] used the approach for the study of a granular ceramic, tungsten carbide (WC). Utilizing continuum and mesoscale modeling tools, it was shown that the measured behavior was strongly dependent upon the shear strength of the material, both at the continuum or mesoscale, but not on the bulk compaction properties (i.e. crush response) of the material.

Mesoscale modeling in which the critical length scale is resolved has been used extensively in the study of granular and other porous materials. Early work by Benson (c.f. [16]) utilized idealized geometries (i.e. circles or spheres) and simple constitutive laws within Eulerian “hydrocodes” to provide insight into the behavior at the grain scale under shock loading. More recently Borg and Vogler [17–19] have studied the shock loading of granular WC in-depth utilizing two- and three-dimensional simulations of relatively large domains. However, Eulerian codes do not treat inter-particle

✉ M. Behzadinasab
behzadi@utexas.edu

¹ Department of Aerospace Engineering and Engineering Mechanics, The University of Texas at Austin, Austin, TX 78712, USA

² Sandia National Laboratories, Livermore, CA 94550, USA

³ Engility Corporation, San Antonio, TX 78228, USA

⁴ Hildebrand Department of Petroleum and Geosystems Engineering, The University of Texas at Austin, Austin, TX 78712, USA

⁵ Fiat Chrysler Automobiles, Detroit, MI 48215, USA

friction or fracture in physically realistic ways. Some mesoscale modeling work [20, 21] has been done utilizing Lagrangian finite element, which can treat inter-particle interactions more realistically. Nevertheless, Dwivedi and co-workers were not able to include particle fracture in their simulations due to the difficulties associated with incorporating it in finite element models. Further, finite element codes are not well-suited to problems involving very large local deformations, requiring remeshing or other approaches to avoid numerical instabilities and mesh tangling. In a couple of investigations [22, 23], an integral reformulation of continuum mechanics known as peridynamics [24] has been used for mesoscale simulations because the peridynamic formulation is well-suited to handling fracture.

The relative importance of phenomena such as inter-particle contact, particle fracture, and local inelastic deformation may change for different problem geometries as well as for variations in driving velocity or energy. For example, penetration problems may be controlled by one phenomenon at low velocities and another at high velocities, while planar shock loading may have a different dependence. The perturbation decay configuration represents a loading condition that shares common features with the planar shock case as well as the penetration case, thus providing a useful test case for mesoscale modeling approaches and an interesting means by which to examine the role of different mechanisms. Further, the perturbation decay experiment is well-suited to mesoscale modeling due to the periodicity of the problem in one direction, so that only one or a few wavelengths needs to be modeled, as well as the nominally zero strain in the other transverse direction. As additional experimental data become available, the continuum and Eulerian-based mesoscale models [14] as well as the Lagrangian peridynamics-based mesoscale model considered here can be evaluated more thoroughly. In this study, we utilize the peridynamic mesoscale model to simulate the perturbation decay experiment as a means to examine the role of inter-particle contact, friction, and particle fracture in an attempt to understand localized phenomena that are not directly observable in the experiments. This is done through parametrically varying the contact friction and fracture material properties of the granular material and studying their effects on the perturbation decay.

Peridynamics

Silling [24, 25] introduced the peridynamic theory which is a continuum reformulation of the classical equation of motion, aiming to represent the mechanics of continuous and discontinuous media using a single consistent set of equations. Peridynamics has been mainly utilized in modeling deformations of bodies where discontinuities, i.e. cracks,

are involved. Recall the classical continuum theory of the conservation of momentum

$$\rho \ddot{\mathbf{u}}(\mathbf{x}, t) = \nabla \times \boldsymbol{\sigma}(\mathbf{x}, t) + \rho \mathbf{b}(\mathbf{x}, t),$$

where \mathbf{u} is the *displacement field* and b is a *body force field*. This theorem uses the divergence of the *Cauchy stress* $\boldsymbol{\sigma}$, hence involves spatial derivatives of displacements. Consequently, the classical theory fails where a discontinuity appears, and it requires special numerical treatments. To circumvent the issue completely, the peridynamic theory models the internal forces exerted on a material point by considering all its interactions with its neighboring points within a finite distance; thus, it is a *nonlocal* theory. The original formulation of the peridynamic equation of motion is

$$\rho \ddot{\mathbf{u}}(\mathbf{x}, t) = \int_{\mathcal{H}(\mathbf{x})} \mathbf{f}(\mathbf{u}(\mathbf{x}', t) - \mathbf{u}(\mathbf{x}, t), \mathbf{x}' - \mathbf{x}) dV_{\mathbf{x}'}, \quad (1)$$

$$+ \rho \mathbf{b}(\mathbf{x}, t),$$

where \mathbf{f} is a *pairwise bond force density*, and $\mathcal{H}(\mathbf{x})$ is the *family set* containing all the neighbors of \mathbf{x} , which is typically a sphere with radius δ called *horizon*. The *bond-based* version of peridynamics (1) was found later to have some shortcomings [26, 27], most notably it was limited to a Poisson's ratio of 1/4 in three dimensions. The original representation suffers from an oversimplifying assumption that the pairwise force potential between two material points only depends on the relative displacement of the two points and is independent of all other conditions. A more generalized form of the theory was later proposed by Silling et al. [27], known as the *state-based* peridynamics

$$\rho \ddot{\mathbf{u}}(\mathbf{x}, t) = \int_{\mathcal{H}(\mathbf{x})} [\underline{\mathbf{T}}[\mathbf{x}' - \mathbf{x}][\mathbf{x}, t] - \underline{\mathbf{T}}[\mathbf{x} - \mathbf{x}'][\mathbf{x}', t]] dV_{\mathbf{x}'}, \quad (2)$$

$$+ \rho \mathbf{b}(\mathbf{x}, t),$$

in which $\underline{\mathbf{T}}$ is defined as the peridynamic *force vector state*, which maps vectors (bonds) into vectors (forces). The angle brackets in this equation indicate the bonds on which the force state operates. This state-based generalization allows for neighboring bonds to interact with each other and eliminates the shortcomings of the original equation. Due to this advantage, we use the state-based peridynamics in this work.

A *linear peridynamic solid* (an elastic peridynamic material) [27] is defined by a strain energy of the form

$$W = \frac{k\theta^2}{2} + \frac{15\mu}{2m} \int_{\mathcal{H}(\mathbf{x})} \underline{\omega}(\underline{e}^d)^2 dV_{\mathbf{x}'}. \quad (3)$$

which results in the following functional form for the force state. Note that for brevity \mathbf{x} , \mathbf{x}' , and t are dropped from the equations.

$$\underline{\mathbf{T}} = \underline{t} \underline{\mathbf{M}}, \quad \underline{t} = \frac{-3p}{m} \underline{\omega x} + \frac{15\mu}{m} \underline{\omega e^d}, \quad p = -k\theta. \quad (4)$$

In these equations, μ and k are the shear and bulk moduli, $\underline{\mathbf{M}}$ is the unit vector pointing from the deformed position of \mathbf{x} to the deformed position of \mathbf{x}' , \underline{x} is the length of the undeformed bond

$$\underline{x}[\mathbf{x}' - \mathbf{x}] = |\mathbf{x}' - \mathbf{x}|,$$

$\underline{\omega}$ is an *influence function* that defines the degree of interactions of material points, and m is the *weighted volume* of a material point that is a scalar defined by

$$m = \int_{\mathcal{H}(\mathbf{x})} \underline{\omega x}^2 dV_{\mathbf{x}'}$$

\underline{e}^d is the *deviatoric part* of the *extension scalar state* \underline{e}

$$\underline{e}^d = \underline{e} - \underline{e}^i, \quad \underline{e} = \underline{y} - \underline{x}, \quad \underline{e}^i = \frac{\theta \underline{x}}{3},$$

where \underline{y} is the length of the deformed bond. θ is the *dilatation* of a material point, a scalar-valued function defined by

$$\theta = \frac{3}{m} \int_{\mathcal{H}(\mathbf{x})} \underline{\omega x e} dV_{\mathbf{x}'}$$

A meshfree method [28] has been typically employed to solve Eq. (2) for general solid mechanics problems. This discretization results in

$$\rho \ddot{\mathbf{u}}(\mathbf{x}_i, t) = \sum_{j=1}^k [\underline{\mathbf{T}}(\mathbf{x}_i, t) \langle \mathbf{x}_j - \mathbf{x}_i \rangle - \underline{\mathbf{T}}(\mathbf{x}_j, t) \langle \mathbf{x}_i - \mathbf{x}_j \rangle] \Delta V_j + \rho \mathbf{b}(\mathbf{x}_i, t) \quad \forall i = 1, 2, \dots, N,$$

where \mathbf{x}_i represents a discrete material point (node), \mathbf{x}_j is a material point within the neighborhood of \mathbf{x}_i , k is the number of all the nodes within $\mathcal{H}(\mathbf{x})$, and N is the total number of nodes within the peridynamic body of interest.

Damage Model

Material failure is modeled through *irreversible* bond breakage [29]. Bond stretch is defined as

$$s = \frac{|\eta| - |\xi|}{|\xi|},$$

in which $|\eta|$ and $|\xi|$ are the bond length in the *current* and *reference* configuration, respectively. According to the *critical stretch failure criterion*, a peridynamic bond breaks irreversibly when its stretch exceeds a critical value s_0 called the *critical stretch* that is a function of the strain energy release rate G_0 an experimentally measurable quantity [28]

$$s_0 = \sqrt{\frac{5G_0}{9k\delta}}.$$

After a bond fails, it can no longer sustain loading; hence, its force must be carried by its neighboring bonds, which triggers a local softening material response. Consequently, this can lead to an evolution of damage in which broken bonds coalesce. Eventually, with sufficient continued loading of the material, the coalescence of failed bonds becomes a fracture which can propagate through the body. It must be pointed out that this failure model works better in tension than in compression, hence damage in problems involving large negative mean stresses becomes complicated due to contact effects.

Local damage ϕ at a point \mathbf{x} is defined as

$$\phi(\mathbf{x}, t) = 1 - \frac{\int_{\mathcal{H}} \underline{v}(\mathbf{x}, t) \langle \mathbf{x}' - \mathbf{x} \rangle dV_{\mathbf{x}'}}{\int_{\mathcal{H}} dV_{\mathbf{x}'}}$$

where \underline{v} is an *indicator state*, i.e.

$$\underline{v} = \begin{cases} 0, & \text{if } s \geq s_0, \\ 1, & \text{otherwise.} \end{cases}$$

In this sense, $0 \leq \phi \leq 1$, with 0 representing a virgin material point and 1 representing a point being completely damaged, i.e. having lost all its connections with the points it was initially interacting with.

Contact Model

A common approach to modeling contact in peridynamics is the *short-range forces* approach of Silling and Askari [28]. In this model contact force is analogous to repulsive elastic forces. When material points from two distinct bodies approach each other and the relative distance between them r falls below the *contact radius* r_c , the contact force activates, i.e.

$$f_c = \begin{cases} C(r_c - r) \Delta V_1 \Delta V_2, & \text{if } r \leq r_c \\ 0, & \text{otherwise,} \end{cases} \quad (5)$$

where $C = 18k/\pi\delta^5$. Contact friction is also incorporated by Coulomb’s friction law.

Self-Contact After Bond Breakage

In our initial results [30] the shock was not being transferred to the material for small values of the critical stretch.

We suspected that the primary factor behind this happening must be the non-physical overlap of grain sub-particles after the grain is fractured. To avoid the matter interpenetration, we implemented a contact force between nodes of the same granular particle after their bond is broken. Rather than explicitly tracking the grain surfaces, we adopted an approach same as the short-range forces contact model (5), which helped to avoid *numerical* interpenetration.

Peridigm

We used Peridigm to simulate the shock wave perturbation decay experiment. Peridigm [31] is an open-source peridynamics code originally developed at Sandia National Laboratories, used primarily to simulate dynamic problems in solid mechanics involving material failure. Peridigm is built upon Sandia's Trilinos project [32] and provides a platform for large-scale parallel peridynamics simulations. It is also capable of modeling contact for transient dynamics analyses.

Simulation Setup

There were several preprocessing steps to create random distributions of grains packed to prescribed densities. The details of generating these computational realizations are given in the following sections.

Geometry

For clarity purposes, the following terms are defined: *particle* is a single material grain, *node* refers to a peridynamics node/element/point used in calculations, and x , y , and z -direction dimensions are called *width*, *depth*, and *thickness*, respectively.

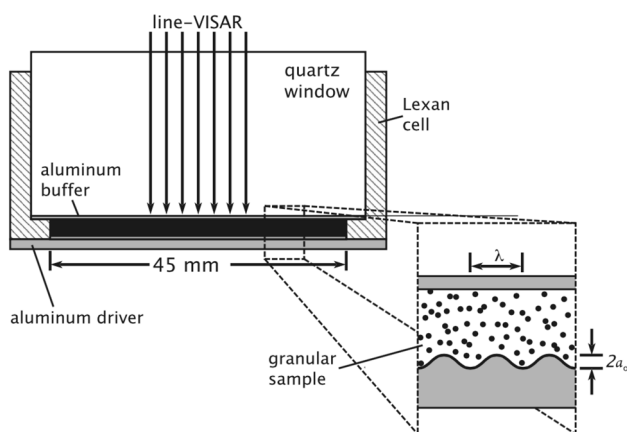


Fig. 1 Schematic of the shock wave perturbation experiments conducted by Vogler [14]

The motivating experiment, illustrated in Fig. 1, involved a driver impact plate with a prescribed upward constant velocity. The plate face was shaped by a sinusoidal cross-section with an amplitude a_0 of 0.25 mm and a wavelength λ of 2 mm. In those experiments, particles with diameter size of 20–32 μm were studied, and the width of the sample was nominally 45 mm.

In this work, for the simulations to be computationally manageable, a two-dimensional, plane-strain approximation was chosen for linear elastic, circular particles with diameter of 30 μm . The final geometry, shown in Fig. 2, was two wavelengths (4 mm) wide by 2.6 mm deep. In order to prevent the particles from translating out to the sides prematurely, physical side wall boundaries were placed at each end of the driver.

Figure 3 illustrates the node arrangement over the field. Each particle was discretized with regards to two directions, across its diameter (r -direction) and perpendicular to its diameter (θ -direction). First, 6 nodes were placed uniformly across a diameter, and then the remainder of nodes were placed discretely along the θ -direction in a near-uniform spacing. A Voronoi technique was used based on the distance between nodes to calculate their associated volume (mass). A sinusoidal driver 5 nodes deep and one node thick was positioned on the bottom of the field. Similarly,

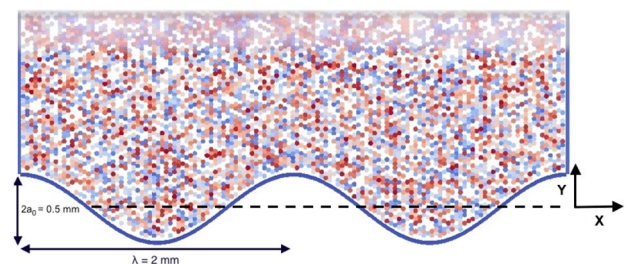


Fig. 2 Initial configuration of the simulation. Shocks are driven from bottom to top. Colors assigned to individual particles are only for visualization purposes. (Color figure online)

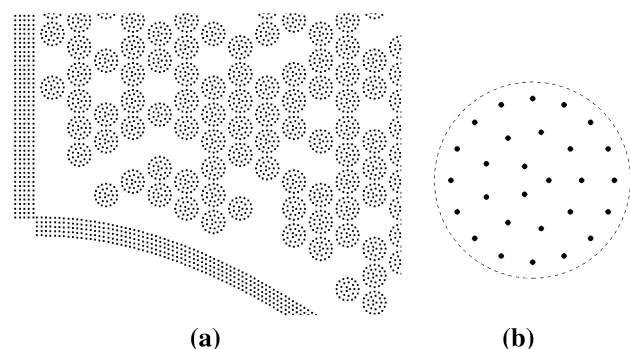


Fig. 3 Node arrangement within **a** the system and **b** a single particle

bounding walls of 5 nodes width and one node thickness were placed at the other edges of the domain. Uniform node spacing for the walls and driver, equal to the average node spacing across the particle diameter, was chosen. The radius of contact for short range forces was chosen slightly smaller than the effective radii of the nodes ($r_c = 0.95 \Delta x_{\text{avg}}$) to make sure that the contact forces are not initially active. The peridynamic horizon size was chosen to be three times the average node spacing, making it equal to a particle radius $\delta = 15 \mu\text{m}$.

A peridynamic node interacts with its neighbors within the same granular particle through the material model (4) before their bond is broken and by means of the self-contact model (5) after the bond breakage. No bond is considered between nodes of different particles, or between nodes of the driver/walls and nodes of the particles; however, they can still interact via the contact model (5) when they are in contact. An influence function is adopted with a uniform value of 1 inside the neighborhood and 0 outside.

Initialization

In order to obtain the initial configuration of the simulation shown in Fig. 2, a field of hexagonally close packed particles one node deep was first initialized. This gives the optimal packing density for circular particles. Particles were then removed randomly until the desired bulk density was achieved. However, it was found that the resulting arrangement led to significant bias and anomalous behavior in the velocity/displacement wave front as shown in Fig. 4a. The

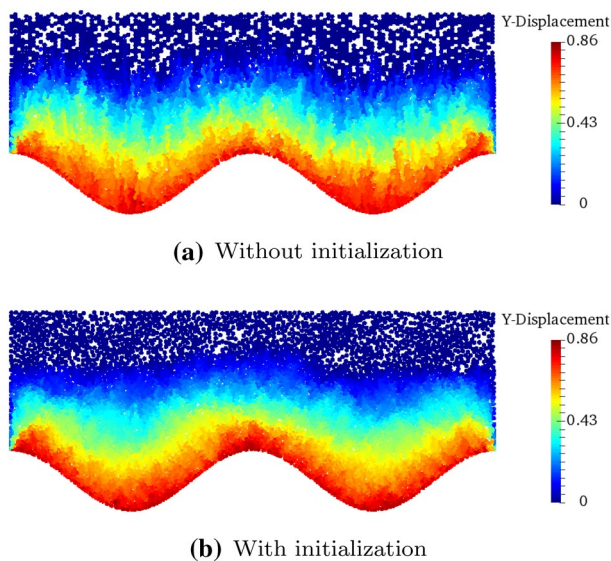


Fig. 4 Importance of the initialization pre-processing step to less biased wave motion. The figures show nodal y -displacements as a result of the driver impact scenario **a** without and **b** with the initialization step

figure shows y -displacement contours driven by the rippled flyers, with and without the initialization pre-processing step.

To achieve a less biased particle arrangement, we used a process similar to that used by Borg and Vogler [17] and in subsequent studies for generating initial particle arrangements. After the random removal step, we prescribed the particles with initial random velocities while enclosed by fixed boundaries (same as the physical bounding walls described in the previous section). Then the simulation was ran for a set period of time such that friction damps out most of the kinetic energy of the particles and the system approaches equilibrium. Material deformation was allowed during the initialization step, but damage was not. The resulting configuration was used as the initial condition in the primary simulations. Figure 5 shows the particle arrangement before and after the initialization step. There is some clumping of particles as seen in Fig. 5b, as would be natural in physical particle settling. The new particle arrangement resulted in less biased velocity and displacement wave fronts as shown in Fig. 4b.

All the numerical simulations were conducted on the Stampede supercomputer at Texas Advanced Computing Center (TACC). Approximately 220,000 peridynamic nodes constituted a case study, whose simulation run lasted about 12 h on 3 Stampede nodes (48 cores). A 3-D simulation of

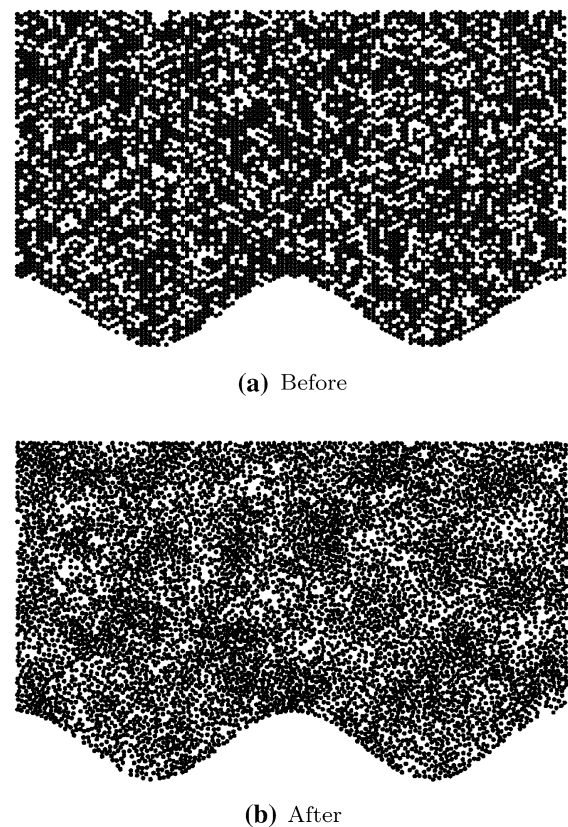


Fig. 5 Particle arrangement before and after the initialization

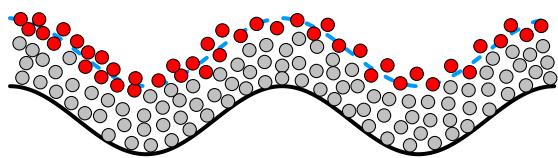


Fig. 6 Schematic of *sine* curve fitting for which the newly moving particles, shown by red color, are found. Grey particles were already moving upward. (Color figure online)

the same problem (with 5 layers of granular particles) would be approximately 200 times more computationally expensive.

Post Processing

Displacement, velocity, and damage were recorded for each node at the end of each time step. In order to determine the perturbation amplitude, the approach of monitoring each particle introduced by Vogler et al. [23] was modified as follows. At the center of each particle a single Lagrangian tracer was placed with its velocity being monitored. When the tracer velocity became larger than half of the driver velocity, the particle was considered to be in motion. As shown in Fig. 6, the positions of those newly moving particles that started to move within a specified time interval δt were used for the sinusoidal wave fit. Choosing too small a time interval would result in not having sufficient particles to obtain a valid fit. On the other hand, sampling over too long a time would result in an inaccurate wave shape. A value of $\delta t = 40$ ns was selected as a compromise between these. Using a least square curve fit function, a cosine curve of the form

$$A \cos\left(\frac{2\pi x}{\lambda}\right) + B$$

was fit to the identified newly moving particles. For each time interval, there is a fit amplitude A and a fit position B .

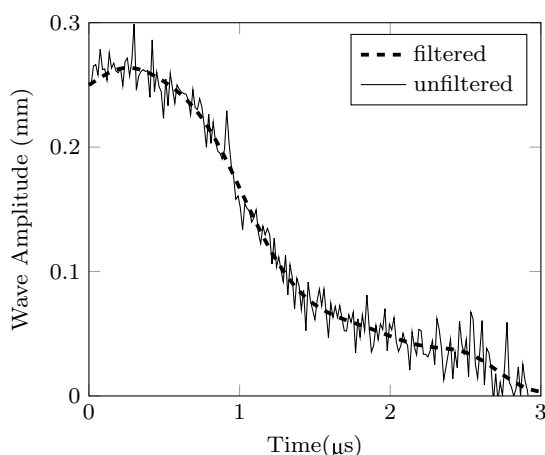


Fig. 7 Data filtering process

To better examine the change in perturbation amplitude, the wavelength was held constant at 2 mm. The corresponding data was filtered using a 4 pole, 3 MHz Butterworth filter as shown in Fig. 7.

The primary purpose of these simulations was to investigate the effects of fracture and friction on the wave propagation. Consequently, variations of the critical stretch (s_0) and the coefficient of friction (μ) at driver velocities (v_{drive}) of 300 m/s and 600 m/s are considered in the simulations. A linear elastic material model is used for particles with density of 2.65 g/cm³, Young's modulus of 170 GPa, and Poisson's ratio of 0.17. The granular particles occupy 55% of the volume.

Results and Discussion

The overall observation made from the simulation results is that there are generally two extreme cases that occur depending on how fast the wave amplitude decays. Before moving on to the sensitivity analysis, an example for each of these cases are discussed. Information about the parameters used in these two case studies are provided in Table 1. Figure 8 displays contours of velocity in the y -direction throughout the simulation. Comparing Fig. 8a–c with Fig. 8d–f reveals that the perturbed wave propagates much faster in *Case B* than *Case A*. Interpreting the damage contours shown in Fig. 9 can help to understand the physics behind this occurrence. It is observed that the s_0 value is too small in *Case A* that as the wave travels, every node becomes completely damaged. On the other hand, the situation is completely different in *Case B* where only the particles near the driver (and some near the side walls, due to the boundary effects) have failed, and negligible damage has occurred elsewhere. With damage and failure happening in the form of grain crushing or fracture, energy is dissipated. Because the s_0 value is smaller in *Case A*, particles are more brittle and the propagating wave causes more damage compared to *Case B*, which in turn produces more surface area for friction to occur, leading to even more energy dissipation.

The quantitative information about the kinetic, potential (strain), and total energy of the granular particles for the two cases are provided in Fig. 10. The total energy is computed by the summation of the strain energy, calculated from (3), and the kinetic energy of the particles. It is learned that granular particles in *Case A* are so crushed that there is negligible strain energy in the system—averaged 8×10^{-5} J in *Case A*

Table 1 Parameters used in the two discussed sample cases

Case	v_{drive} (m/s)	μ	s_0
A	300	0.2	0.005
B	300	0.2	0.03

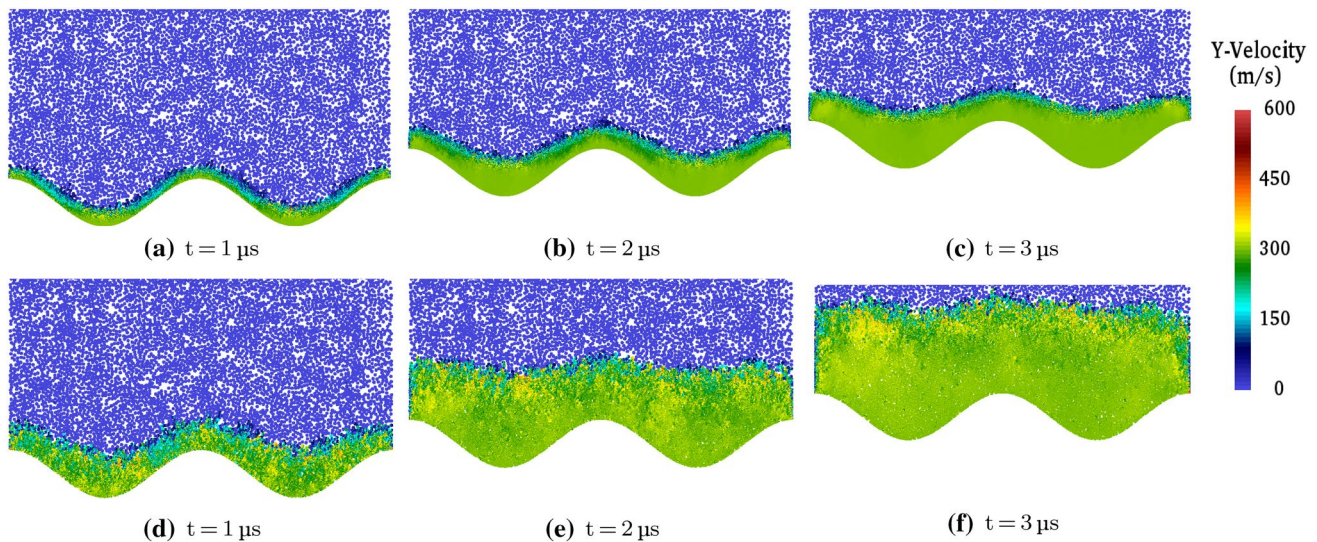


Fig. 8 Contour plots of nodal y-velocity: **a–c** Case A **d–f** Case B. (Color figure online)

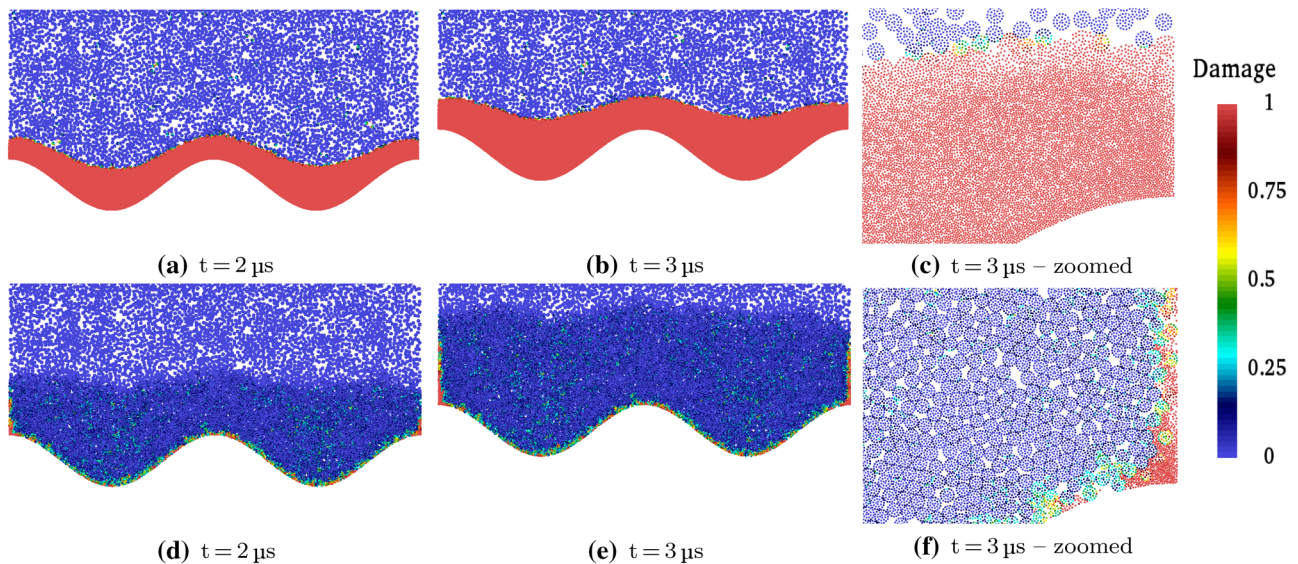


Fig. 9 Contour plots of nodal damage: **a–c** Case A **d–f** Case B. Zoomed windows at the bottom right sides of **b** and **e** are shown in **c** and **f**, respectively. (Color figure online)

compared to 1.5×10^{-2} J in Case B. Also, the more energy dissipation involved in Case A resulted in a significantly lower kinetic energy and hence total energy of the grains.

The perturbation features in Case A are compared to Case B in Fig. 11. Not only does the wave propagate faster in Case B but also its amplitude decays faster. Looking closer to the velocity profiles in the two cases, as shown in Fig. 12, can help understanding the physics behind this phenomenon. The wave travels faster in Case

B and a more scattered velocity profile develops in the x direction—mainly due to a non-uniform distribution of voids. Consequently, a stronger dispersion happens and the wave amplitude decays faster in that case. In contrast, particles along the wave front appear to have closer vertical speeds in Case A. It happens because the grains are so crushed that their sub-grains along the shock front move all together, thus the void-related effects are damped.

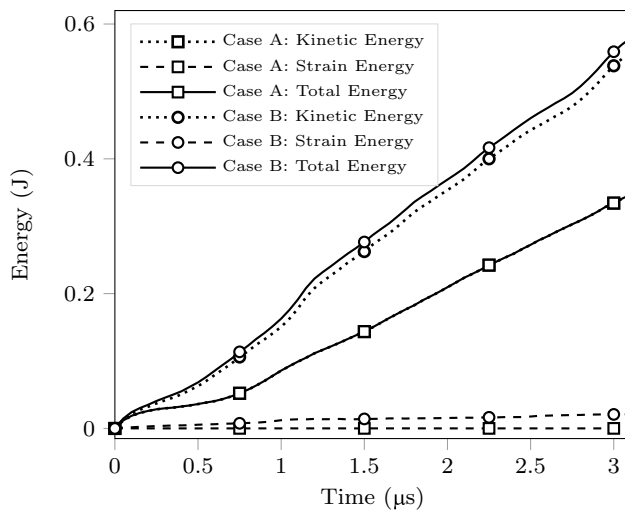
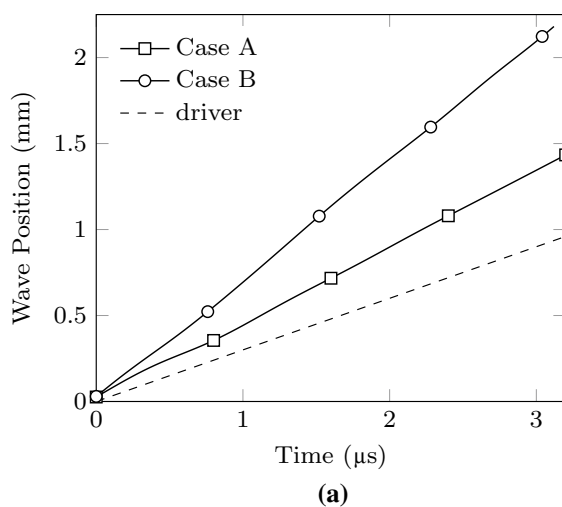


Fig. 10 Evolution of energy of the granular particles in *Case A* and *Case B*. Damage mechanism resulted in a more dissipation of energy in *Case A* as a result of a lower critical stretch. Severe damage in *Case A* resulted in a near-zero strain energy of the grains (of order 10^{-4} J), hence the total and kinetic energies in that case overlap. Only a portion of the data points are shown by markers, for visualization purposes

Spatial Refinement

We examine the effect of mesh refinement on one of the case studies. Here we reduce the horizon and the node spacing at the same time by keeping horizon three times the average node spacing. The base case contains 3 nodes across a granular particle radius. Other discretizations involve 4, 5, 6, 7, and 8 nodes across a radius. The total



number of PD nodes within an individual particle for different discretizations are provided in Table 2.

As shown in Fig. 13, simulated velocity contours are in good agreement for different discretizations. Damage, shown in Fig. 14, is more sensitive to the refinement as there seems to be a larger damaged area in the most refined case. That behavior, however, is expected because as the horizon is reduced, damage is more localized. Experimental data can help to determine a physically meaningful value for the horizon.

Wave amplitudes, shown in Fig. 15, are somewhat affected by the discretization, yet the trends are similar. *Average shock wave velocity* (v_{shock}) is defined as the slope of the line fitted through the wave displacement vs. time plot. Provided in Table 2, the average shock speeds do not change significantly with discretization. Since we view these simulations as a way to gain physical insight into the effects of damage and contact friction on wave characteristics, rather than an attempt to match experimental results, for computational expediency we utilize the base case discretization with 6 nodes across a particle diameter, $0.5 \mu\text{m}$ cell size, and a horizon of $1.5 \mu\text{m}$.

Initial Realization

To study the effect of initial particle arrangements, simulation results of a particular case with different initial randomizations are presented. The resulting wave amplitudes, shown in Fig. 16, are somewhat sensitive to the initial configuration but qualitatively show similar behavior. This is consistent with the results from Vogler [14] where fairly large variability in perturbation decay was seen for different realizations. To reduce the variability, those simulations were run with

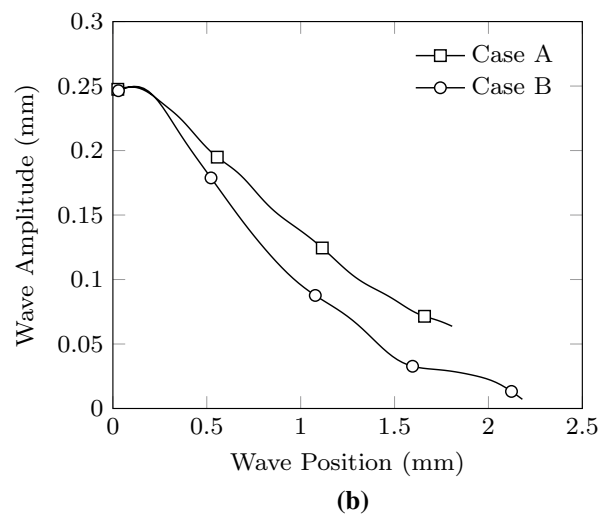


Fig. 11 The perturbed wave propagates faster and its amplitude decays more quickly in *Case B* compared to *Case A*. Only a portion of the data points are shown by markers, for visualization purposes

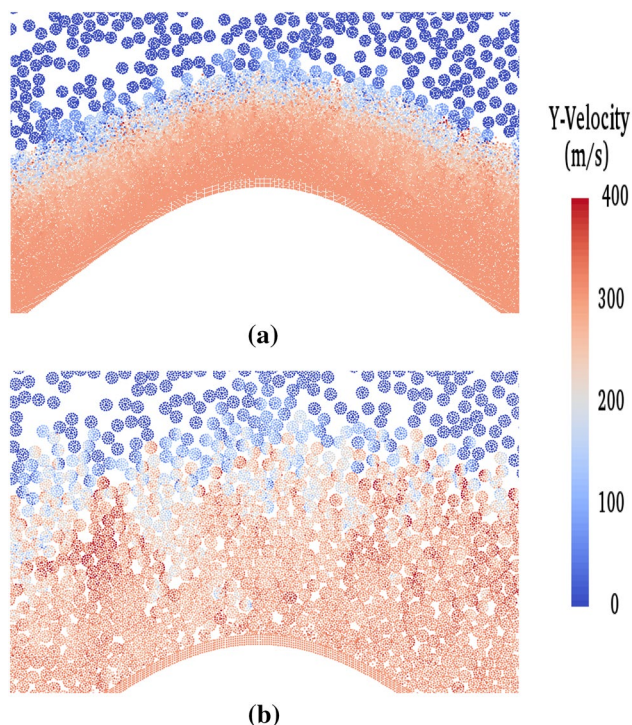


Fig. 12 Snapshots of nodal velocities at the instance the wave front reaches the position 1 mm. The wave arrives at the same location faster in *Case B* and exhibits a more scattered particle velocity profile. Zoomed windows from the center of the setup are shown here. **a** *Case A*, **b** *Case B*. (Color figure online)

Table 2 Mesh refinement effects on a case with $v_{drive} = 600$ m/s, $\mu = 0.2$, and $s_0 = 0.02$

Number of nodes across particle radius	Number of nodes within particle	v_{shock} (m/s)
3	28	929
4	50	932
5	78	942
6	113	949
7	154	939
8	201	942

four wavelengths. However, the average shock velocities, provided in Table 3, are very close. With respect to the intent of this work, a single initial particle configuration was randomly chosen for sensitivity analysis.

Sensitivity Analysis and Discussion

The sensitivity of the perturbed wave characteristics to the values of the critical stretch and the coefficient of friction was examined next. All the cases were simulated for two different driver velocities, 300 and 600 m/s, s_0 was varied from 0.005 to 0.1 at steps of 0.005 for $\mu = 0.2$ and 0.5. Furthermore, a variation of μ from 0.1 to 1 at steps of 0.1 was considered for s_0 values of 0.01, 0.02, 0.03, and 0.05.

The effect of the critical stretch variation on the wave amplitude is shown in Fig. 17. It is observed that for smaller values of s_0 , its variation would considerably affect the wave amplitude, with higher critical stretches resulting in faster decays. However, for both of the driver velocities a value of s_0 exists (0.025 for 300 m/s and 0.06 for 600 m/s here) such that further increase of s_0 has negligible effect on the wave amplitude. Those threshold values correspond to when the particles are so tough that any added increase in their strength has little impact on their behavior.

Figure 18 displays the effect of variation of μ on the wave amplitude. For both driver velocities, while the wave amplitude generally increases with friction—which is expected in a continuous medium as well—it is not very sensitive to μ . This finding becomes more interesting when the result is compared to our earlier study [30], where the self-contact between the nodes after bond-breakage were ignored and the results indicated that the variation of μ had stronger influence on the wave amplitude. Our previous study showed that for small values of s_0 the front wave velocity was very close to the driver velocity, i.e. the perturbed wave did not propagate far. This occurrence was due to the non-physical overlap of fractured grain sub-particles (nodes). In the most non-physical case, when a grain was completely fractured, all of its nodes could have overlapped into a single point. As might be expected under strong compression, our results also confirm

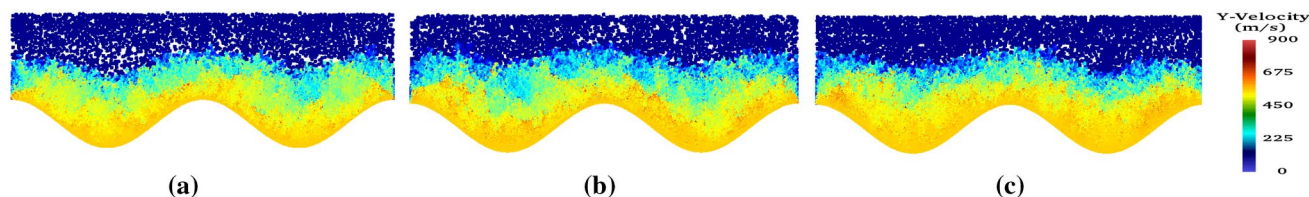


Fig. 13 Contour plots of nodal y-velocity at the same instance of the simulation for different numbers of nodes across each particle radius; $v_{drive} = 600$ m/s, $\mu = 0.2$, and $s_0 = 0.02$. **a** 3 nodes across radius, **b** 6 nodes across radius, **c** 8 nodes across radius. (Color figure online)

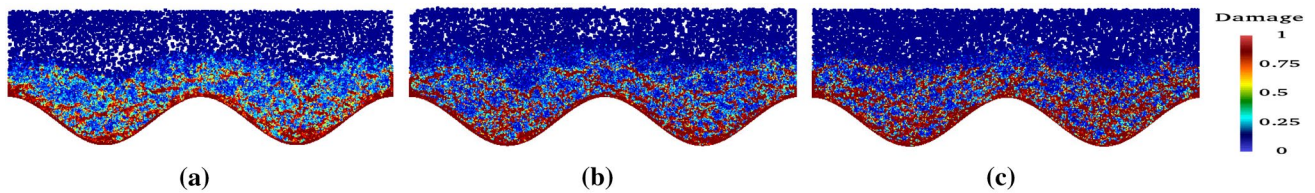


Fig. 14 Contour plots of nodal damage at the same instance of the simulation for different numbers of nodes across each particle radius; $v_{drive} = 600\text{m/s}$, $\mu = 0.2$, and $s_0 = 0.02$. **a** 3 nodes across radius, **b** 6 nodes across radius, **c** 8 nodes across radius. (Color figure online)

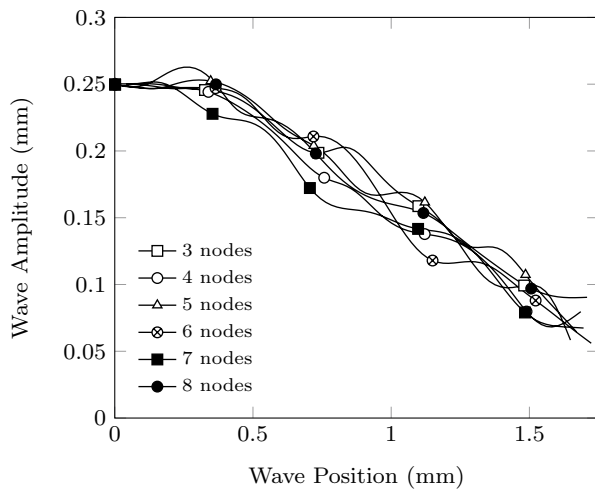


Fig. 15 Effect of nodal refinement on wave amplitude; a case study with $v_{drive} = 600\text{ m/s}$, $\mu = 0.2$, and $s_0 = 0.02$. Only a portion of the data points are shown by markers, for visualization purposes

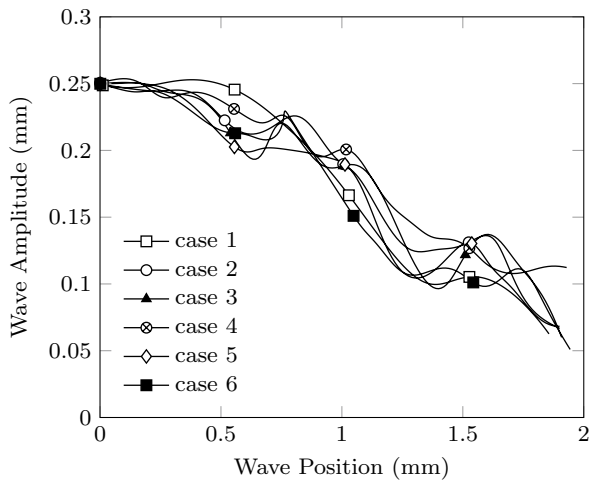


Fig. 16 Wave amplitude in different random realizations; a case study with $v_{drive} = 600\text{ m/s}$, $\mu = 0.2$, and $s_0 = 0.015$. Only a portion of the data points are shown by markers, for visualization purposes

that the matter of self-contact for a severely fractured particle cannot be neglected.

Table 3 Average shock velocity in different realizations; $v_{drive} = 600\text{ m/s}$, $\mu = 0.2$, and $s_0 = 0.015$

Case	v_{shock} (m/s)
1	893
2	899
3	889
4	912
5	908
6	890

To explain why the wave characteristics do not significantly change with μ , we speculate that intact particles interact mainly through the equivalent of central forces, even in the perturbed shock front. Friction effects would be greater realized if there were more particle sliding or rotation, perhaps as in a pressure-shear configuration. Another possibility is that the *roughness* of the particle surfaces caused by individual discretization leads the grains to lock up rather than slide. Additional work is needed to better understand the roles of contact friction in perturbation decay and other phenomena in granular materials.

Figure 19 shows the average shock wave velocities for all the simulations. It is notable that not only the wave speed would increase with s_0 , but it also grows with μ . This may be a counter intuitive result as it may seem that more friction would induce more energy dissipation and should decrease the perturbation velocity, yet the opposite occurs. To investigate the physics behind this phenomenon, we design an impact scenario between two granular particles shown in Fig. 20. Suppose that particle 2 is initially moving upward with velocity V_0 before it comes to contact with the other particle. In order to facilitate the analysis, we simplify the phenomena by assuming two rigid particles come in a purely elastic impact in the normal direction with no damage involved. Sliding is allowed in the tangential direction.

In this situation, the particle velocities will change as a result of the normal and tangential forces acting during the impact. The tangential force is limited by the friction coefficient

$$F_t \leq \mu F_n.$$

The conservation of momentum is utilized to calculate the resultant forces. Suppose that the mass of both particles is m .

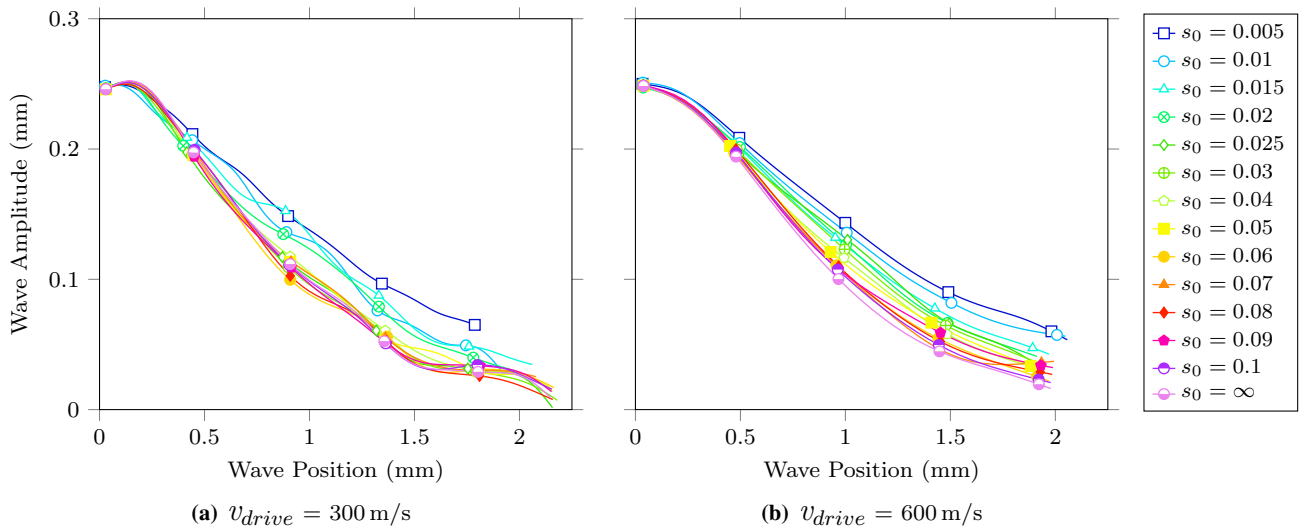


Fig. 17 Effect of variation of the critical stretch on wave amplitude as a function of time, where $\mu = 0.2$. Only a portion of the data points are shown by markers, for visualization purposes. (Color figure online)

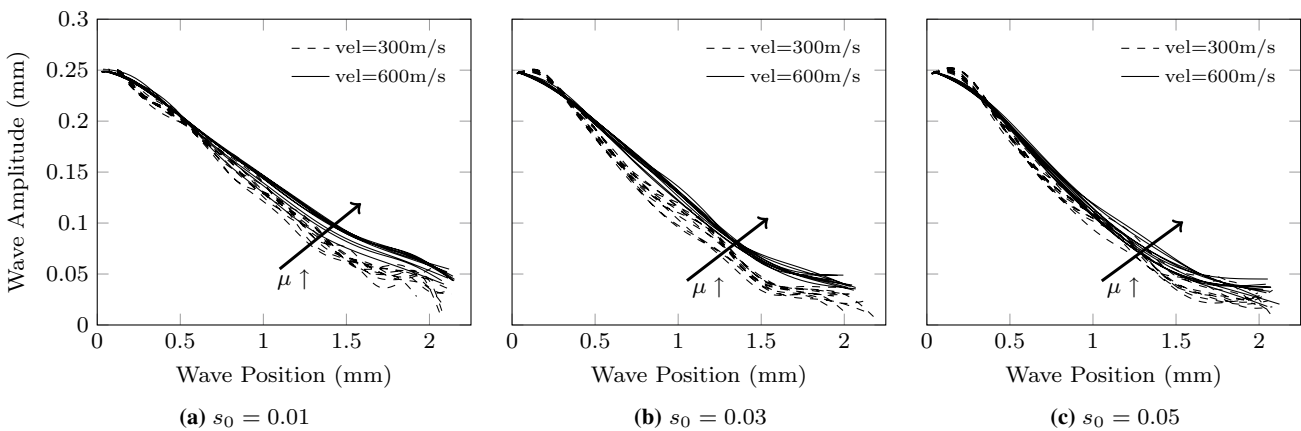


Fig. 18 Effect of the coefficient of friction variation on wave amplitude; for each driver velocity, different lines correspond to different values of μ , which is varied from 0.1 to 1

$$mV_{1n} + mV_{2n} = mV_0 \cos \theta. \tag{6}$$

$$mV_{1t} + mV_{2t} = mV_0 \sin \theta. \tag{7}$$

Using the assumption of elastic contact in the normal direction (the coefficient of restitution = 1)

$$V_{1n} - V_{2n} = V_0 \cos \theta. \tag{8}$$

By solving (6) and (8) the normal velocities after impact are found to be

$$V_{1n} = V_0 \cos \theta, \quad V_{2n} = 0. \tag{9}$$

The frictional forces are active at the beginning. Friction will be present throughout the impact if there exists relative

tangential velocity between the particles. If the particles tangential velocities become the same at some point during the impact, sliding will not occur anymore.

Case 1. If enough friction is involved, both particles can reach the same tangential velocity after the impact, i.e. $V_{1t} = V_{2t}$. Thus, using (7)

$$V_{1t} = V_{2t} = \frac{1}{2} V_0 \sin \theta. \tag{10}$$

Using (9) and (10) the vertical component of V_1 is then

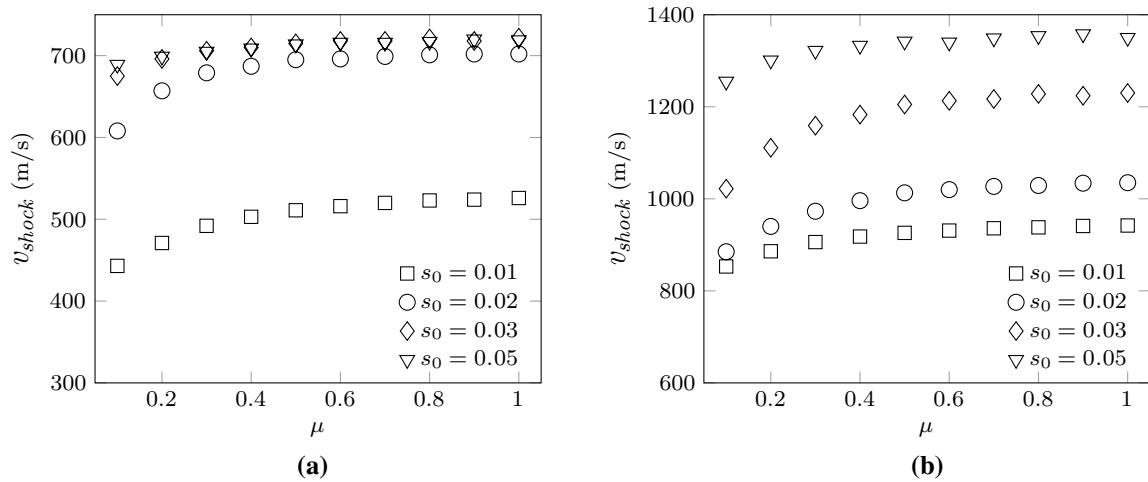


Fig. 19 Effect of variation of the coefficient of friction and the critical stretch on shock wave velocity **a** $v_{drive} = 300$ m/s and **b** $v_{drive} = 600$ m/s

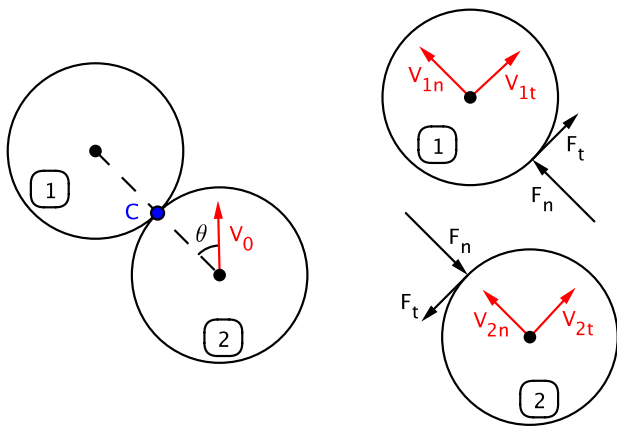


Fig. 20 An oblique central impact between two rigid grains with one being initially stationary and the other one moving upward with velocity V_0 . In this simplified scenario, the normal and tangential forces acting during the impact result in the final velocities of the particles V_1 and V_2 . θ is the angle of contact; with regards to the direction of tangential force here $0 \leq \theta \leq \pi/2$. (Color figure online)

$$\begin{aligned}
 V_{1y} &= V_{1n} \cos \theta + V_{1t} \sin \theta, \\
 &= V_0 \cos^2 \theta + \frac{1}{2} V_0 \sin^2 \theta, \\
 &= V_0 \left(1 - \frac{1}{2} \sin^2 \theta \right).
 \end{aligned}$$

As there is no strain energy for rigid particles, kinetic energy governs the energy of the system. The total energy before the impact is

$$E_0 = \frac{1}{2} m V_0^2.$$

The energy of the system after the impact becomes

$$\begin{aligned}
 E &= \frac{1}{2} m \left(\frac{1}{2} V_0 \sin \theta \right)^2 + \frac{1}{2} m \left((V_0 \cos \theta)^2 + \left(\frac{1}{2} V_0 \sin \theta \right)^2 \right), \\
 &= \frac{1}{2} m V_0^2 \left(1 - \frac{1}{2} \sin^2 \theta \right).
 \end{aligned}$$

The dissipated energy can be calculated as

$$\begin{aligned}
 \Delta E &= E_0 - E, \\
 &= \frac{1}{4} m V_0^2 \sin^2 \theta.
 \end{aligned}$$

Case 2. $V_{1t} < V_{2t}$ at the end of impact. In the limiting case $F_t = \mu F_n$ during the impact, hence

$$\begin{aligned}
 V_{1t} &= \mu V_{1n}, \\
 &= \mu V_0 \cos \theta.
 \end{aligned} \tag{11}$$

Comparing (10) with (11) the condition here is that

$$\begin{aligned}
 \mu V_0 \cos \theta &< \frac{1}{2} V_0 \sin \theta, \\
 \Rightarrow \mu \cos \theta &< \frac{1}{2} \sin \theta.
 \end{aligned} \tag{12}$$

Substituting (11) in (7) results in

$$V_{2t} = V_0 (\sin \theta - \mu \cos \theta).$$

The energy of the system after impact is calculated to be

$$\begin{aligned}
 E &= \frac{1}{2} m (V_0 (\sin \theta - \mu \cos \theta))^2 \\
 &\quad + \frac{1}{2} m ((V_0 \cos \theta)^2 + (\mu V_0 \cos \theta)^2), \\
 &= \frac{1}{2} m V_0^2 (1 + 2\mu^2 \cos^2 \theta - 2\mu \sin \theta \cos \theta).
 \end{aligned}$$

Therefore, the dissipated energy is

$$\Delta E = \mu m V_0^2 \cos \theta (\sin \theta - \mu \cos \theta).$$

Making use of the condition (12)

$$\Delta E > \frac{1}{2} \mu m V_0^2 \cos \theta \sin \theta. \quad (13)$$

The vertical component of V_1 can be calculated using (9) and (11)

$$V_{1y} = V_0 \cos^2 \theta + \mu V_0 \cos \theta, \sin \theta = V_0 \cos \theta (\cos \theta + \mu \sin \theta). \quad (14)$$

This dynamics-based analysis confirms that while increasing the friction results in a more dissipation of the energy of system—see (13)—it results in a faster transfer of the wave front—see (14). There is also a limit on the role friction can play—see (12). Depending on the angle of contact, there is a threshold friction coefficient that further increase of that would not be effective. This is also observed in Fig. 19 that initially the increase in μ has significant impact on the shock velocity but becomes less tangible in higher μ 's.

It is further perceived from Fig. 19 that the shock velocity reaches a plateau in high s_0 and μ values. A potential speculation is that an increase in s_0 and μ leads to stronger interactions between particles, thus the assembly of the particles could behave more like a solid. In high values of those two parameters, the remaining difference of the system with a solid body would be the spacing between particles, which would lead to a decline in the wave speed. The slow down occurs as particles would collide at speeds related to their particle velocity as they cross the gaps among them, and the shear stresses generated by friction as particles slide past each other.

Conclusions

The peridynamic framework has been used to incorporate inter-granular contact and friction, and intra-granular fracture, to study those effects on dynamic behavior of granular materials in a shock wave perturbation decay experiment. Our results indicate that friction does not change significantly the spatial response of the wave amplitude in this experiment, but it becomes an important factor in the shock front velocity as our results indicate that friction would generally increase the wave speed. It is further confirmed that after a grain is fractured, the self-contact between its material points cannot be ignored. Our main conclusion is that intra-granular fracture, a phenomenon ignored in most computational investigations of granular materials, plays a large role in the dynamic response. For these brittle materials, the damage mechanism dissipates energy by releasing stored strain energy, leading to new surfaces. Then, friction forces acting on the produced surfaces would dissipates even more energy.

Acknowledgements We greatly appreciate the financial support from the AFOSR MURI Center for Materials Failure Prediction through Peridynamics and Sandia National Laboratories. Sandia National Laboratories is a multi-mission laboratory managed and operated by National Technology and Engineering Solutions of Sandia, LLC., a wholly owned subsidiary of Honeywell International, Inc., for the U.S. Department of Energy's National Nuclear Security Administration under contract DE-NA0003525.

References

1. Sakharov AD, Zaidel RM, Mineev VN, Oleinik AG (1965) Experimental investigation of the stability of shock waves and the mechanical properties of substances at high pressures and temperatures. *Sov Phys JETP* 9:1091–1094
2. Mineev VN, Savinov EV (1967) Viscosity and melting point of aluminum, lead, and sodium chloride subjected to shock compression. *Sov Phys JETP* 25:411–416
3. Mineev VN, Zaidel RM (1968) The viscosity of water and mercury under shock loading. *Sov Phys JETP* 27:874–878
4. Miller GH, Ahrens TJ (1991) Shock-wave viscosity measurement. *Rev Mod Phys* 63(4):919–948
5. Mineev VN, Funtikov AI (2004) Viscosity measurements on metal melts at high pressure and viscosity calculations for the Earth's core. *Phys-USpekhi* 47:671–686
6. Mineev VN, Funtikov AI (2005) Measurements of the viscosity of water under shock compression. *High Temp* 43:141–150
7. Mineev VN, Funtikov AI (2006) Measurements of the viscosity of iron and uranium under shock compression. *High Temp* 44:941–949
8. Liu FS, Yang MX, Liu QW, Chen JX, Jing FQ (2005) Shear viscosity of aluminum under shock compression. *Chin Phys Lett* 22:747–749
9. Li-Peng F, Fu-Sheng L, Xiao-Juan M, Bei-Jing Z, Ning-Chao Z, Wen-Peng W, Bin-Bin H (2013) A fiber-array probe technique for measuring the viscosity of a substance under shock compression. *Chin Phys B* 22:108301
10. Li Y, Liu F, Ma X, Li Y, Yu M, Zhang J, Jing F (2009) A flyer-impact technique for measuring viscosity of metal under shock compression. *Rev Sci Instrum* 80(1):013903
11. Ma XJ, Liu FS, Zhang MJ, Sun YY (2011) Viscosity of aluminum under shock-loading conditions. *Chin Phys B* 20:068301
12. Li YL, Liu FS, Zhang MJ, Ma XJ, Li YL, Zhang JC (2009) Measurement on effective shear viscosity coefficient of iron under shock compression at 100 GPa. *Chin Phys Lett* 26:038301
13. Ma X, Liu FS, Sun Y, Zhang M, Peng X, Li Y (2011) Effective shear viscosity of iron under shock-loading condition. *Chin Phys Lett* 28:044704
14. Vogler TJ (2015) Shock wave perturbation decay in granular materials. *J Dyn Behav Mat* 1:370–387
15. Vogler TJ, Behzadinasab M, Rahman R, Foster JT (2016) Perturbation decay experiments on granular materials. Sandia National Laboratories Report 2016
16. Benson DJ (1997) The numerical simulation of the dynamic compaction of powders. In: Davison L, Horie Y, Shahinpoor M (eds) High-pressure shock compression of solids IV: response of highly porous solids to shock loading. Springer, New York, pp 233–255
17. Borg JP, Vogler TJ (2008) Mesoscale calculations of the dynamic behavior of a granular ceramic. *Int J Solids Struct* 45:1676–1696
18. Borg JP, Vogler TJ (2009) Aspects of simulating the dynamic compaction of a granular ceramic. *Modell Simul Mater Sci Eng* 17:045003

19. Borg JP, Vogler TJ (2013) Rapid compaction of granular materials: characterizing two and three-dimensional mesoscale simulations. *Shock Waves* 23:153–176
20. Dwivedi SK, Teeter RD, Felice CW, Gupta YM (2008) Two dimensional mesoscale simulations of projectile instability during penetration in dry sand. *J Appl Phys* 104:083502
21. Dwivedi SK, Pei L, Teeter RD (2015) Two-dimensional mesoscale simulations of shock response of dry sand. *J Appl Phys* 117:085902
22. Lammi CJ, Vogler TJ (2012) Mesoscale simulations of granular materials with peridynamics. In: Elert ML (ed) *Shock compression of condensed matter-2011*. American Institute of Physics, New York, pp 1467–1470
23. Vogler TJ, Borg JP, Grady DE (2012) On the scaling of steady structured waves in heterogeneous materials. *J Appl Phys* 112:123507
24. Silling SA (2000) Reformulation of elasticity theory for discontinuities and long-range forces. *J Mech Phys Solids* 48:175–209
25. Silling SA (2003) Dynamic fracture modeling with a meshfree peridynamic code. In: Bathe KJ (ed) *Computational fluid and solid mechanics*. Elsevier, Amsterdam, p 641644
26. Foster JT, Silling SA, Chen WW (2010) Viscoplasticity using peridynamics. *Int J Numer Meth Eng* 81:1242–1258
27. Silling SA, Epton M, Weckner O, Xu J, Askari E (2007) Peridynamic states and constitutive modeling. *J Elast* 88:151–84
28. Silling SA, Askari E (2005) A meshfree method based on the peridynamic model of solid mechanics. *Comput Struct* 83:1526–1535
29. Silling SA, Askari E (2004) Peridynamic modeling of impact damage. In: *ASME/JSME 2004 pressure vessels and piping conference*. American Society of Mechanical Engineers, pp 197–205
30. Behzadinasab M, Vogler TJ, Foster JT (2018) Modeling perturbed shock wave decay in granular materials with intra-granular fracture. In: *AIP conference proceedings of the 20th APS-SCCM*, vol 1979
31. Parks ML, Littlewood DJ, Mitchell JA, Silling SA (2012) *Peridigm users guide*. Sandia National Laboratories Report 2012
32. Heroux MA, Bartlett RA, Howle VE, Hoekstra RJ, Hu JJ, Kolda TG, Salinger AG (2005) An overview of the Trilinos project. *ACM TOMS* 31:397–423